Gravity Referenced Elevation Encoder Development

R. E. Goddard
Guidance and Control Section

Recent progress in the development of a gravity-sensor-based instrument for determining the elevation angle of DSN antennas is described. The benefits of such a system include the capability to locate the Gravity Referenced Elevation Encoder (GREE) directly on the primary reflector (thus bypassing structural flexure and deformation error sources), anticipated lower maintenance costs compared to the present gimbal encoders, direct replaceability or supplementation of the present gimbal encoders and the utilization of off-the-shelf components to construct the GREE. This article includes a description of the nominal GREE design. Test results on a laboratory breadboard model are given. Rigid-body dynamics of the GREE are derived and the simulated performance in response to measured antenna vibrations is given.

I. Introduction

Large structure ground-based antennas are subject to pointing errors which prevent achieving the full designed performance of the antennas [1–3]. Major error sources are gravity sag, thermal gradients and hysteresis of the primary reflector and its supporting structure. Therefore, the mechanical boresight of the primary reflector is not directly observable from the angle encoders on the axes' gimbals because of the large amount of structural separation. As an alternative to gimbal measurements, an instrument capable of sensing the Earth's gravity vector may be placed directly on the primary reflector to bypass the structural error sources. Knowledge of the gravity vector in antenna coordinates defines the elevation angle. In Section II, a Gravity Referenced Elevation Encoder (GREE) is described and the results of recently completed laboratory proof-of-concept tests of noise and long term drift are given. The rigid body dynamics of the GREE are derived in Section III and the nominal controller design is given. Simulated performance of the GREE in a DSN disturbance environment is detailed in Section IV.

II. Gravity Referenced Elevation Encoder

The GREE is constructed of all off-the-shelf components. Figure 1 is a pictorial of the GREE. The major components are the brushless DC motor, optical encoder, and accelerometer. The accelerometer is mounted via an adapter block onto the optical encoder rotor shaft. The opposite end of this shaft is rotated by the motor until the accelerometer output is nulled. The angular rotation required to null the accelerometer is read on the optical encoder. This angle is the elevation angle of the GREE itself. Knowledge of the calibration matrix between the GREE and the primary reflector mechanical boresight yields the antenna elevation angle. A block diagram of the GREE is shown in Fig. 2 and the laboratory unit is shown in Fig. 3. It is anticipated that thermal stabilization will be utilized in the field deployable unit to prevent temperature residual bias drift of the accelerometer. However, the laboratory model has neither heaters nor thermal insulation.

Long term stability of the sensor bias determines the time between recalibrations. Test results (Fig. 4) over 27

days indicate a 3σ of 0.8 mdegs after detrending. A trend of 0.2 mdeg is apparent in the data. The suspected cause is cyclic microtilting of the laboratory pier. The test was limited to an accelerometer on hand; however a superior version of the accelerometer, available at a modest cost increase, is expected to reduce the long term drift by 50 percent per manufacturer's specifications. Further, the drift may not be linear, which means that extrapolation of the test results is not applicable. Although the results are encouraging, longer duration tests should be completed to characterize the bias drift. A Hewlett-Packard spectrum analyzer recorded the short term noise spectrum. The rms noise is 0.32 mdeg at a 3.63-Hz sampling resolution and an accelerometer bandwidth of 250 Hz.

III. Rigid Body Dynamics

In this section, the GREE rotational dynamics are derived. The accelerometer is a torque-balanced pendulous mass sensor as shown in Fig. 5. The torque τ is developed by internal control electronics to maintain the angular position of the mass in accelerometer body coordinates. The amount of torque required is $\tau = m\,g\,l\,\sin\theta$ and the output is zero when the accelerometer sensitive axis is aligned with gravity.

The GREE dynamics are derived utilizing a two degree-of-freedom planar model. One degree of freedom represents the rotation axis of the optical encoder and the second degree of freedom is the accelerometer rotation axis. Figure 6 details the dynamic model where for simplicity the misalignments are assumed zero, i.e., the calibration matrix is the identity transformation. The following quantities are defined:

ε = elevation angle

θ_1 = rotor shaft angle with respect to gravity

$x_i,\ y_i$ = location of center of mass of member i, $i = 1,\ 2$

$x_0,\ y_0$ = rotor axis of rotation

COM_i = center of mass of member i, $i = 1, 2$

k_1 = distance of accelerometer axis from rotor COM_1

θ_I = accelerometer pendulous mass angle with respect to accelerometer case

θ_2 = accelerometer pendulous mass angle with respect to gravity

$fx_i,\ fy_i$ = resultant coupling forces on rotational axis i, $i = 1, 2$

g = gravitational constant

l_i = COM_i offset from rotational axis i, $i = 1, 2$

I_i = inertia of member i about COM_i, $i = 1,\ 2$

The axis of rotation of the rotational member consisting of the optical encoder shaft, accelerometer, and actuator rotor (see Fig. 1) is given by the coordinates x_0, y_0. The kinematics of the system defined in Fig. 6 are ($s_i = \sin\theta_i, c_i = \cos\theta_i$):

$$x_1 = x_0 + l_1 c_1 \qquad x_2 = x_1 + k_1 c_1 + l_2 c_2$$

$$y_1 = y_0 + l_1 s_1 \qquad y_2 = y_1 + k_1 s_1 + l_2 s_2$$

Twice time differentiating the above equations yields:

$$\left.\begin{aligned}
\ddot{x}_1 &= \ddot{x}_0 - l_1\left(\dot{\theta}_1^2 c_1 + \ddot{\theta}_1 s_1\right)\\
\ddot{y}_1 &= \ddot{y}_0 + l_1\left(-\dot{\theta}_1^2 s_1 + \ddot{\theta}_1 c_1\right)\\
\ddot{x}_2 &= \ddot{x}_0 - l_1\left(\dot{\theta}_1^2 c_1 + \ddot{\theta}_1 s_1\right) - k_1\left(\dot{\theta}_1^2 c_1 + \ddot{\theta}_1 s_1\right) - l_2\left(\dot{\theta}_2^2 c_2 + \ddot{\theta}_1 s_2\right)\\
\ddot{y}_2 &= \ddot{x}_0 + l_1\left(-\dot{\theta}_1^2 s_1 + \ddot{\theta}_1 c_1\right) + k_1\left(-\dot{\theta}_1^2 s_1 + \ddot{\theta}_1 c_1\right) + l_2\left(-\dot{\theta}_2^2 s_2 + \ddot{\theta}_2 c_2\right)
\end{aligned}\right\} \quad (1)$$

The translational dynamics are

$$\left.\begin{aligned} m_1\ddot{x}_1 &= f_{x_1} - f_{x_2} + m_1 g \qquad m_1\ddot{y}_1 = f_{y_1} - f_{y_2} \\ m_2\ddot{x}_2 &= f_{x_2} + m_2 g \qquad m_2\ddot{y}_2 = f_{y_2} \end{aligned}\right\} \tag{2}$$

Solving for the coupling forces (f_{x_i}, f_{y_i}) in terms of the translational accelerations and substituting out these accelerations via Eq. (1) yields

$$\left.\begin{aligned} f_{x_1} &= (m_1+m_2)\left[\ddot{x}_0 - l_1\left(\dot{\theta}_1^2 c_1 + \ddot{\theta}_1 s_1\right)\right] - m_2 k_1\left[\dot{\theta}_1^2 c_1 + \ddot{\theta}_1 s_1\right] - m_2 l_2\left[\dot{\theta}_2^2 c_2 + \ddot{\theta}_2 s_2\right] - (m_1+m_2)\,g \\ f_{x_2} &= m_2\ddot{x}_0 - m_2 l_1\left(+\dot{\theta}_1^2 c_1 + \ddot{\theta}_1 s_1\right) - m_2 k_1\left[+\dot{\theta}_1^2 c_1 + \ddot{\theta}_1 s_1\right] - m_2 l_2\left[\dot{\theta}_2^2 c_2 + \ddot{\theta}_2 s_2\right] - m_2 g \\ f_{y_1} &= (m_1+m_2)\,\ddot{y}_0 + (m_1+m_2)\,l_1\left(-\dot{\theta}_1^2 s_1 + \ddot{\theta}_1 c_1\right) + m_2 k_1\left(-\dot{\theta}_1^2 s_1 + \ddot{\theta}_1 c_1\right) + m_2 l_2\left(-\dot{\theta}_2^2 s_2 + \ddot{\theta}_2 c_2\right) \\ f_{y_2} &= m_2\ddot{y}_0 + m_2 l_1\left(-\dot{\theta}_1^2 s_2 + \ddot{\theta}_1 c_1\right) + m_2 k_1\left(-\dot{\theta}_1^2 s_1 + \ddot{\theta}_1 c_1\right) + m_1 l_2\left(-\dot{\theta}_2^2 s_2 + \ddot{\theta}_2 c_2\right) \end{aligned}\right\} \tag{3}$$

The rotational dynamics may now be written and the coupling forces substituted out to arrive at the dynamics in rotational coordinates. The results are

$$\left.\begin{aligned} &\left[I_1 + l_1^2(m_1+m_2) + 2l_1 k_1 m_2 + k_1^2 m_2\right]\ddot{\theta}_1 + \left[(l_1+k_1)\,l_2 m_2\cos(\theta_2-\theta_1)\right]\ddot{\theta}_2 \\ &- \left[(l_1+k_1)\,l_2 m_2\sin(\theta_2-\theta_1)\right]\dot{\theta}_2^2 + l_1 s_1(m_1+m_2)\,g + k_1 s_1 m_2 g \\ &= +l_1 s_1(m_1+m_2)\,\ddot{x}_0 - l_1 c_1(m_1+m_2)\,\ddot{y}_0 + k_1 s_1 m_2\ddot{x}_0 - k_1 c_1 m_2\ddot{y}_0 + \tau_1 - \tau_2 \end{aligned}\right\} \tag{4a}$$

$$\left.\begin{aligned} &\left[(l_1+k_1)l_2 m_2\cos(\theta_2-\theta_1)\right]\ddot{\theta}_1 + \left[(l_1+k_1)l_2 m_2\sin(\theta_2-\theta_1)\right]\dot{\theta}_1^2 \\ &+ \left[I_2 + m_2 l_2^2\right]\ddot{\theta}_2 + l_2 m_2 s_2 g = +l_2 m_2 s_2\ddot{x}_0 - l_2 m_2 c_2\ddot{y}_0 + \tau_2 \end{aligned}\right\} \tag{4b}$$

In the dynamics, the accelerations $(\ddot{x}_0, \ddot{y}_0)$ represent composite motion of the GREE due to antenna vibrations $(\ddot{x}_0', \ddot{y}_0')$ and a jitter on the elevation angle $(\dot{\varepsilon}, \ddot{\varepsilon})$. This is expressed as

$$\ddot{x}_0 = \ddot{x}_0' - l_0(\sin\varepsilon\ \ddot{\varepsilon} + \cos\varepsilon\ \dot{\varepsilon}^2) \tag{5a}$$

$$\ddot{y}_0 = \ddot{y}_0' - l_0(\cos\varepsilon\ \ddot{\varepsilon} - \sin\varepsilon\ \dot{\varepsilon}^2) \tag{5b}$$

where l_0 is the off-axis mounting of the GREE. Table 1 lists the parametric values utilized for the GREE. The values are obtained from actual measurements of the GREE components, vendor specifications, or calculations. The parameter l_0 represents the assumed off-axis mounting of the GREE on the antenna; and the parameter l_1 represents the assumed center-of-mass imbalance on the optical encoder rotor. These two quantities are installation and fabrication constraints, respectively.

The linearized GREE model is shown in Fig. 7. The actuator is modeled in the frequency domain as a simple first-order torque generator:

$$\tau = \frac{\left(\frac{k_\tau}{l}\right)(v - k_v s\theta)}{\left(s + \frac{r}{l}\right)} \tag{6}$$

where k_τ, k_v, r and l are the torque constant, back electromotive force (EMF) constant, coil resistance, and coil inductance, respectively, and s is the complex frequency. The accelerometer model is a second-order critically damped system with an appropriate scale factor (SF). The linearized dynamics of the rotor are derived utilizing $I_2 \ll I_1$:

$$\frac{\theta}{\tau} = \frac{\dfrac{1}{(I_1 + m_1 l_1^2)}}{s^2 + \left(\dfrac{m_1 l_1 g}{I_1 + m_1 l_1^2}\right)} \equiv \frac{k_r}{(s^2 + \omega_0^2)} \tag{7}$$

A generalized model of bearing friction [4], Fig. 8, describes the restoring torque as a function of rotation. This represents the resistance to rotation exhibited by the optical encoder bearing action. The model is characterized by coulomb torque (T_c), the spatial time constant (τ_c), and the material factor (i). All of the curves in Fig. 8 have equal slope ($T_c \backslash \tau_c$) at the origin of the torque-rotation curve and therefore an exponential approximation may be utilized. An analytical torque-rotation curve with hysteresis is shown in Fig. 9. This model is valid for $\dot{\beta} > 0$ and $\dot{\beta} < 0$. The expression for this model utilized in the subsequent simulations is

$$T(\beta) = \operatorname{sgn}(\dot{\beta}) T_c + [T(0) - \operatorname{sgn}(\dot{\beta}) T_c]\left[e^{-(\beta/\tau_c)}\right] \tag{8}$$

where $T(0)$ is the starting torque and β is the angular change from the starting (last reversal) angle. Since a linearized model is required for the controller design, a spring constant is defined by

$$\Delta T = \frac{dT}{d\beta}\Delta\beta = \frac{T_c}{\tau_c}\Delta\beta \equiv k\Delta\beta \tag{9}$$

Table 2 lists values for the GREE components.

The linearized dynamics (Fig. 7) are utilized to compute a controller. The calculations are considerably simplified if higher order modes are neglected. Referring to Table 2, the motor and accelerometer dynamics are widely separated from the plant dynamics. Also combining the back EMF and friction loops into the plant dynamics yields the reduced-order block diagram in Fig. 10. A classical proportional, integral, and derivative (PID) controller is

$$H = b_1 s + b_0 + \frac{b_{-1}}{s} \tag{10}$$

The rotor angle θ_1 is the error signal. If, for example, $\theta_1(\omega) = 0$ for all ω, then $\beta = \varepsilon$, and the system is error free. The controller H must keep θ_1 small. From Fig. 10, the closed-loop error transfer function is

$$\frac{\theta_1}{\varepsilon} = \frac{k k_r s}{s^3 + \left[2\zeta\omega_n + \dfrac{k_\tau SF k_r b_1}{r}\right]s^2 + \left[\dfrac{k_\tau SF k_r b_0}{r} + \omega_n^2\right]s + \left[\dfrac{k_\tau SF k_r b_{-1}}{r}\right]} \tag{11}$$

For simplicity let the closed loop response be three first order responses possessing break frequencies ω_1, ω_2, and ω_3. The controller solution is

$$b_1 = \left[\frac{r}{k_t SF k_r}\right][\omega_1 + \omega_2 + \omega_3 - 2\zeta\omega_n]$$

$$b_0 = \left[\frac{r}{k_t SF k_r}\right][\omega_1\omega_2 + \omega_1\omega_3 + \omega_2\omega_3 - \omega_n^2]$$

$$b_{-1} = \left[\frac{r}{k_t SF k_r}\right][\omega_1\omega_2\omega_3] \tag{12}$$

The PID controller places a zero at the origin in the error transfer function, Eq. (11). For the analytical models used, a constant input will result in zero error. This is desirable since the nominal trajectory of a celestial track has a fundamental period of 1/(86,400) Hz. The error frequency response can be made flat over a particular band. For example, let $\omega_1 = 2\pi(0.01)$ and $\omega_2 = \omega_3 = 2\pi(500)$ rad/sec. The resulting Bode diagram for the error $\theta_1(\omega)$, Fig. 11, is flat from 0.01 to 500 Hz with a minimum error attenuation of -80 dB.

IV. Nonlinear Simulations

The nonlinear equations derived in Section III are utilized to simulate the GREE response to DSN antenna

vibrations. The nonlinear friction model (Fig. 9) is included. Measured vibration data on DSS 14, as given in Fig. 12, are the input. Also included are the effects of angular jitter on the elevation angle $\varepsilon(t)$ at a 20-Hz rate and 0.01-rad amplitude. A fourth-order Runge-Kutta integration at a step size of 10 msec computed the GREE response given in Fig. 13. The expected error is less than 1 mdeg under these conditions.

V. Summary

The present state of development of an inertial instrument for DSN antennas has been described. A breadboard model GREE tested in the laboratory demonstrated acceptable noise and long-term drift characteristics. Rigid body analytical models and simulations have been developed for design and analysis. A nominal controller design maintained the simulated elevation angle error to less than 1 mdeg when driven by measured 70-m antenna vibrations.

The performance of a GREE under actual antenna vibrations can be determined by a field test. Because the GREE will retrofit both mechanically and electrically onto existing antennas, a performance comparison study with the existing gimbal encoders can be designed. The recently completed laboratory demonstration unit can be upgraded for the field test by the addition of heaters, thermal insulation, mechanical mounting hardware and an electrical interface. Prior to the field testing, the analytical model needs to be upgraded to incorporate the dominant flexible modes and the controller upgraded to maintain the desired performance in the specific antenna environment.

References

[1] C. N. Guiar, F. L. Lansing, and R. Riggs, "Antenna Pointing Systematic Error Model Derivations," *The Telecommunications and Data Acquisition Progress Report 42-88*, vol. October–December 1986, Jet Propulsion Laboratory, Pasadena, California, pp. 36–46, February 15, 1987.

[2] K. Abichandani, "Unified Analysis for Antenna Pointing and Structural Error Part 1. Review," *The Telecommunications and Data Acquisition Progress Report 42-73*, vol. January–March 1983, Jet Propulsion Laboratory, Pasadena, California, pp. 40–59, April 15, 1983.

[3] S. Katow, J. J. Cucchissi, K. L. Chuang, R. Levy, J. L. Lansing, F. W. Stoller, and F. Menninger, "Structural Design Options for the New 34 Meter Beam Waveguide Antenna," *The Telecommunications and Data Acquisition Progress Report 42-88*, vol. October–December 1986, Jet Propulsion Laboratory, Pasadena, California, pp. 183–186, February 15, 1987.

[4] P. R. Dahl, "Solid Friction Damping of Mechanical Vibrations," *AIAA Journal*, vol. 14, no. 12, pp. 1675–1688, December 1976.

Table 1. Mass properties for simulation.

Parameter	Value	
Inertia, kg-m^2	$I_1 = 1.28 \times 10^{-2}$	$I_2 = 5.65 \times 10^{-4}$
Mass, kg	$m_1 = 1.02 \times 10^{0}$	$m_2 = 1.20 \times 10^{-4}$
Distance to center of mass, m	$l_1 = 5.00 \times 10^{-3}$	$l_2 = 8.89 \times 10^{-3}$
Distance to accelerometer rotation axis, m	$k_1 = 1.00 \times 10^{-2}$	
Distance to elevation axis, m	$l_0 = 1.00 \times 10^{0}$	
Vibration scale factor, kg-m	$k_x = 5.09 \times 10^{-3}$	
Rotor transfer function, (kg-m^2)$^{-1}$	$k_r = 7.78 \times 10^{1}$	
Rotor transfer function, rad/sec	$\omega_0 = 1.97 \times 10^{0}$	

Table 2. Component mechanical and electrical properties.

Component	Value
Brushless dc motor	
Torque constant, newton-m/ampere	$k_T = 1.91 \times 10^{-1}$
Inductance, henries	$l = 4.32 \times 10^{-2}$
Resistance, ohms	$r = 2.40 \times 10^{1}$
Voltage constant, volts/rad/sec	$k_v = 1.91 \times 10^{-1}$
Half-power frequency, rad/sec	$p_3 = 5.55 \times 10^{2}$
Accelerometer	
Scale factor, volts/rad	$SF = 2.87 \times 10^{2}$
Break frequency, Hz	$p_1, p_2 = 2.00 \times 10^{3}$
Optical encoder friction	
Coulomb torque, newton-m	$T_c = 5.30 \times 10^{-3}$
Spatial constant, rad	$\tau_c = 4.00 \times 10^{-4}$
Spring constant, newton-m/rad	$k = 1.32 \times 10^{1}$

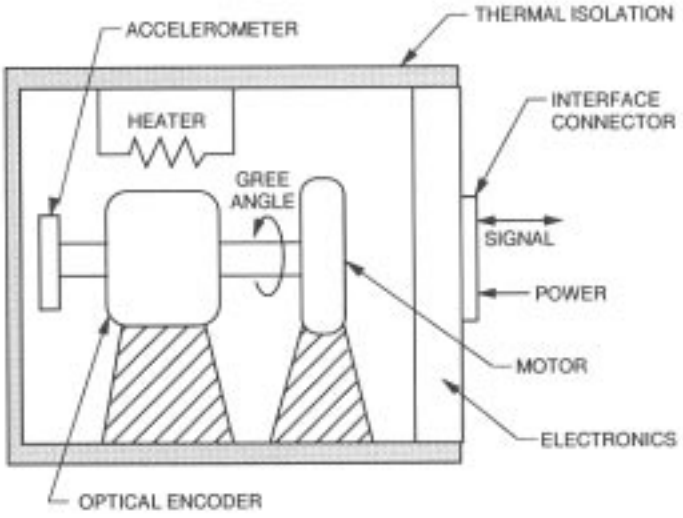

Fig. 1. GREE components.

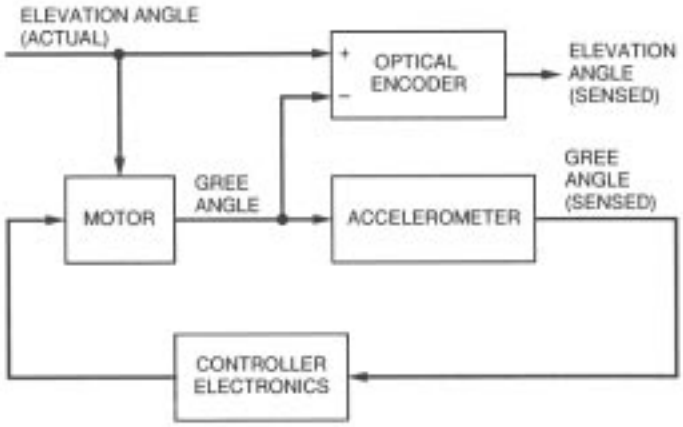

Fig. 2. GREE block diagram.

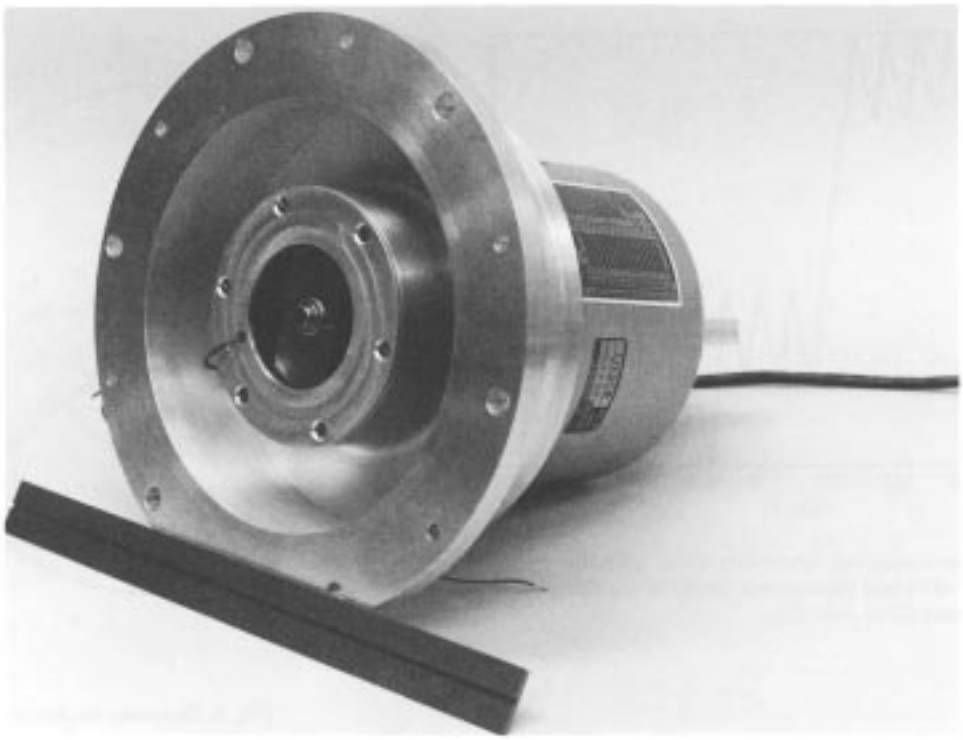

Fig. 3. Laboratory demonstration unit.

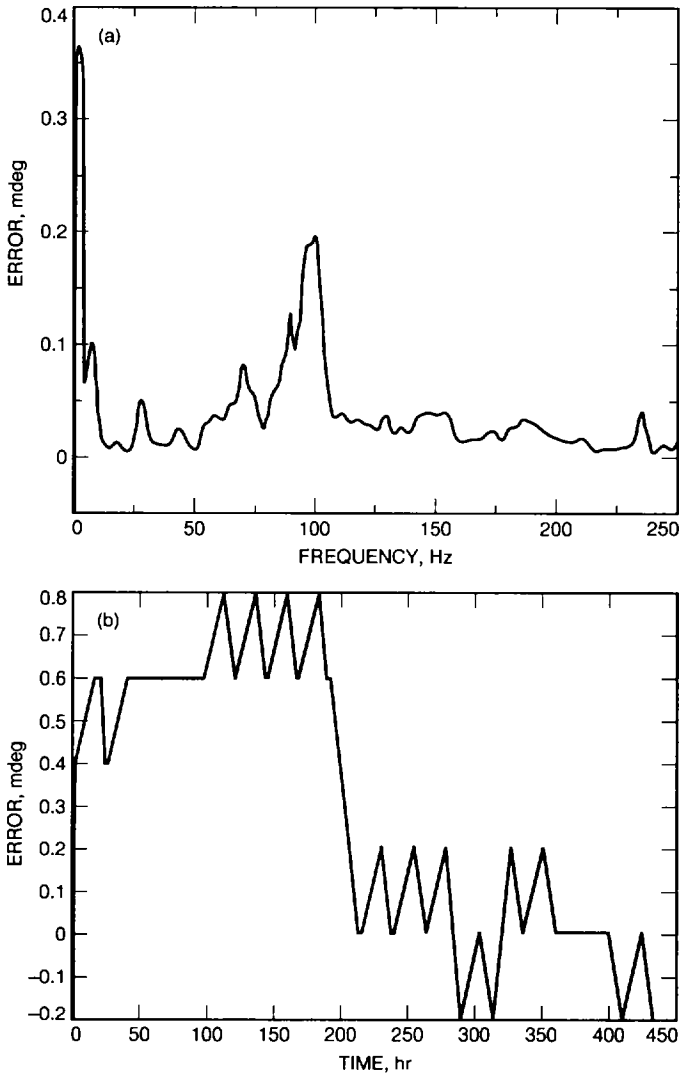

Fig. 4. Accelerometer-measured laboratory data: (a) noise spectrum and (b) 27-day drift test (Substrand QA-2000 accelerometer bias stability test, June 22 to July 17).

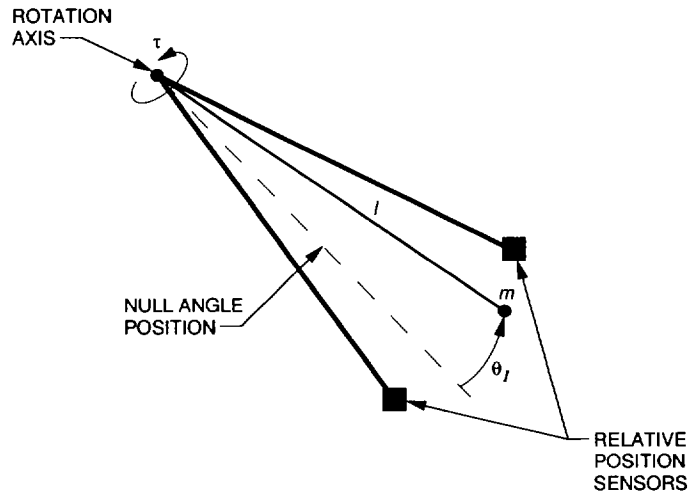

Fig. 5. Accelerometer principle of operation.

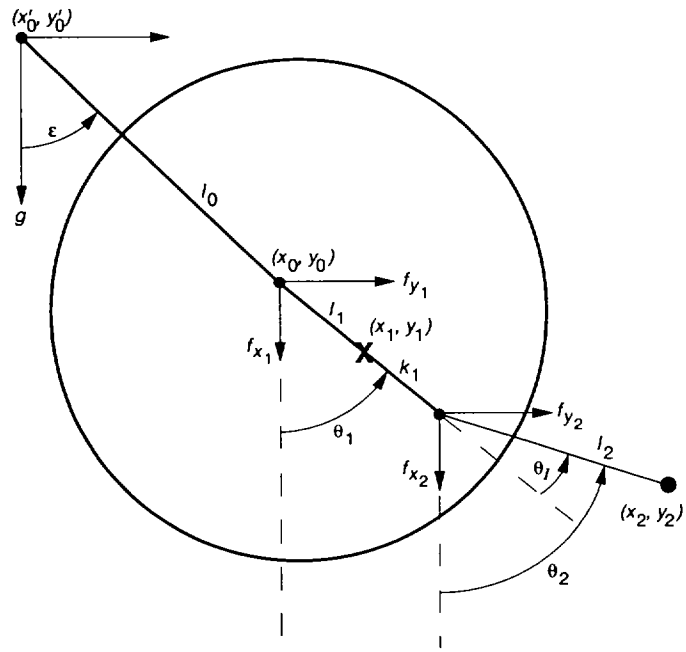

Fig. 6. Dynamic model of GREE.

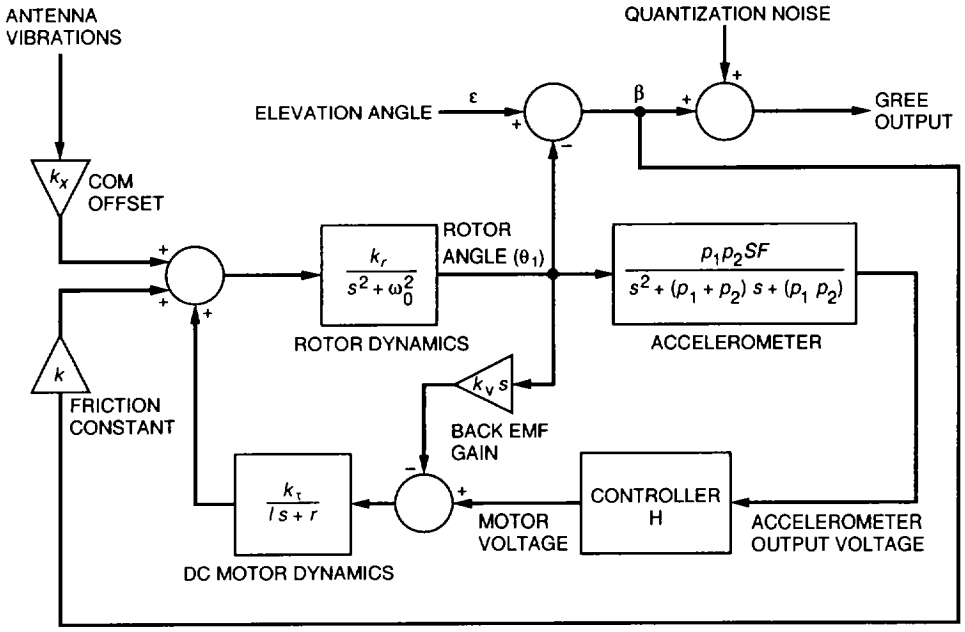

Fig. 7. Linearized dynamics for controller design.

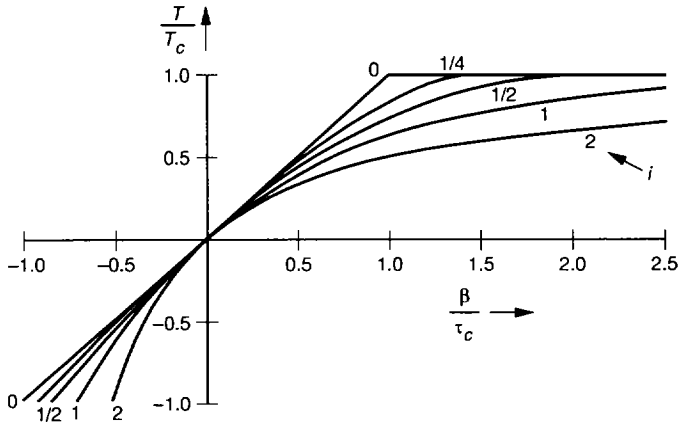

Fig. 8. Generalized force-displacement curve of solid friction damping.

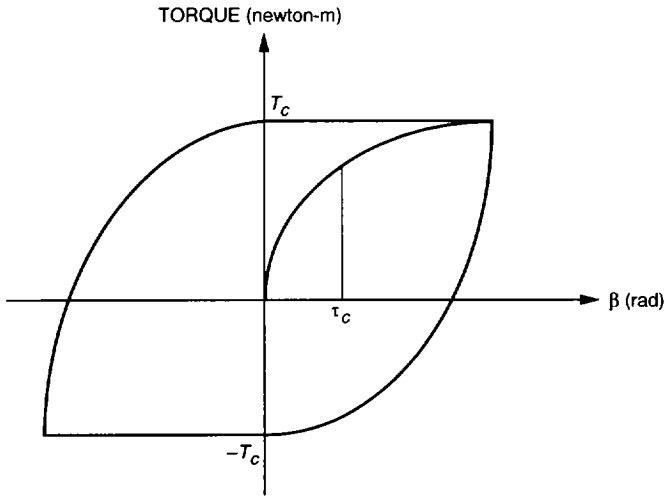

Fig. 9. Torque-rotation curve for linear controller design.

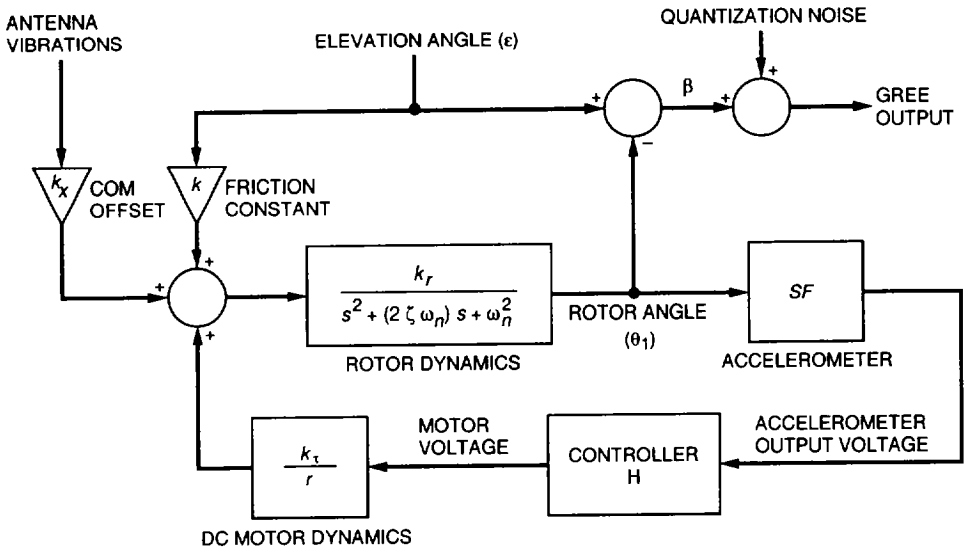

Fig. 10. PID controller and reduced-order GREE model ($\omega_N = 32.2$ rad/sec; $\zeta = 0.002$).

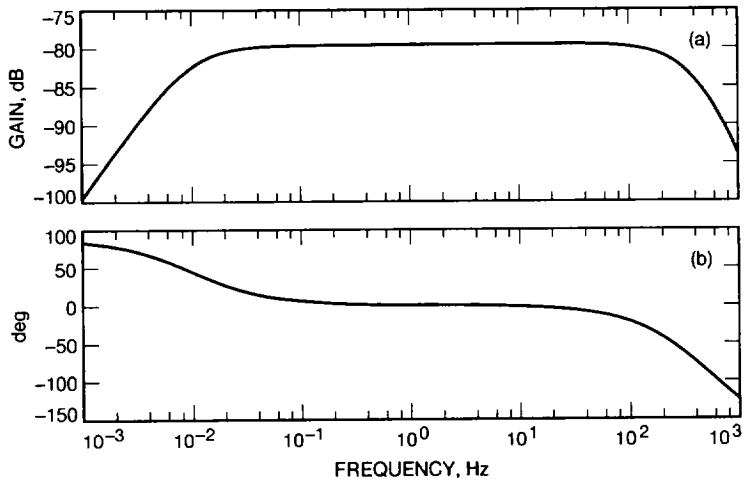

Fig. 11. Error frequency response: (a) error magnitude (small elevation changes) and (b) error phase (small elevation changes).

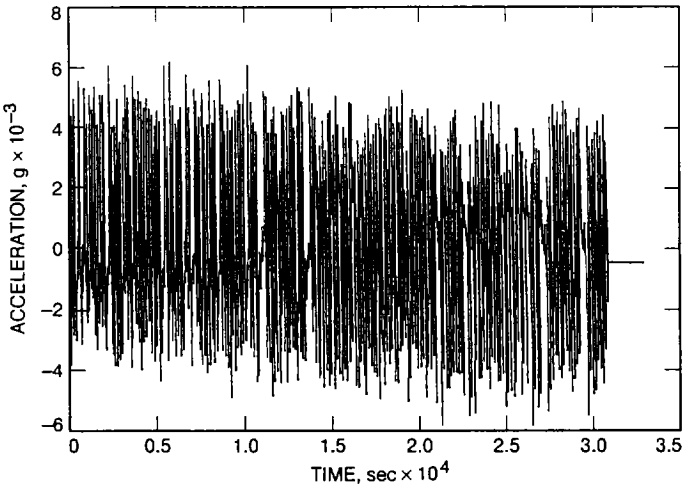

Fig. 12. Measured DSS-14 (70-m) antenna vibration data for simulation.

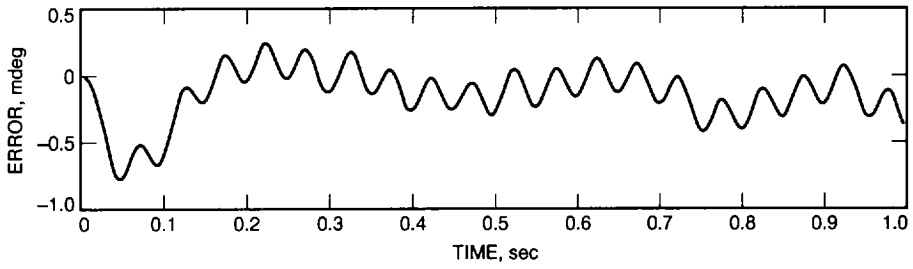

Fig. 13. Simulated GREE response to DSS-14 disturbance environment.